Journal of Materials Research and Technology 31 (2024) 2077–2093

Contents lists available at ScienceDirect

Journal of Materials Research and Technology

journal homepage: www.elsevier.com/locate/jmrt

Comparative analysis of microstructural, compositional, and grazing incidence characteristics of oxide scale on 316L steel: SLM vs. wrought conditions

Alireza Sehat [a], Morteza Hadi [a,*], Taghi Isfahani [a], F. Fernandes [b,c]

[a] Materials Engineering Group, Golpayegan College of Engineering, Isfahan University of Technology, 87717-67498, Golpayegan, Iran
[b] CIDEM, ISEP - Polytechnic of Porto, Rua Dr. António Bernardino de Almeida, 4249-015, Porto, Portugal
[c] University of Coimbra, CEMMPRE, ARISE, Department of Mechanical Engineering, Rua Luís Reis Santos, 3030-788, Coimbra, Portugal

ARTICLE INFO

Handling Editor:P Rios

Keywords:
Oxidation
316L steel
Oxide scale
Selective laser melting
Wrought alloy

ABSTRACT

The aim of this research is to compare the oxidation behavior and characteristics of oxide scale of 316L steel produced by two methods: selective laser melting (SLM) and conventional casting and forming (wrought). To this end, the initial composition and microstructure of samples produced by those methods were first studied. Thermogravimetric analysis (TGA) and long-term isothermal oxidation tests were carried out on the samples and the oxidation kinetics were compared. The oxidized samples were then examined by scanning electron microscopy (SEM), energy dispersive X-ray spectroscopy (EDS) and grazing incidence X-ray diffraction (GIXRD). The results indicated that in the temperature range of 600 °C–900 °C, the oxidation resistance of the SLM alloy is lower than that of the wrought alloy, especially at 800 °C. This is attributed to the combined effect of: i) smaller grain size due to the rapid solidification in the SLM alloy that increases the paths of oxygen penetration, ii) lower presence of chromium and manganese elements in the oxide layer and iii) preferential growth of iron oxide in the form of hillocks on the surface. Surface and cross-section analysis of the oxide layers show that iron oxide is dominant on the surface of the SLM sample at temperatures of 600 °C and 800 °C, and at 800 °C its extended hilly growth leads to significant spallation of the oxide scale and an exponential increase in the oxidation rate. However, at 900 °C, with the formation of a continuous oxide layer containing Fe_2MnO_4 and $CrMnO_4$, the oxidation rate significantly decreases in both alloys.

1. 1- Introduction

Selective Laser Melting (SLM) has emerged as a revolutionary additive manufacturing technique, offering unprecedented flexibility and precision in the production of complex metallic components [1]. Among the myriad of materials used in SLM, the production of 316L steel is of particular importance. A low-carbon variant of stainless steel, 316L steel has exceptional tribological and mechanical properties, making it indispensable in a range of critical applications [2]. Researchers have studied various aspects of 316L produced by selective laser melting (SLM), including its microstructure and mechanical properties [3,4], corrosion resistance [5,6], wear properties [7,8], and fatigue behavior [9,10]. The culmination of these efforts has not only deepened our understanding of the material's behavior, but also paved the way for its widespread adoption in critical sectors such as aerospace, automotive and biomedical engineering [11,12].

Among the many applications that require the use of 316L steel, its oxidation properties at high temperatures stand out as a critical consideration. Extensive research has been devoted to understanding and optimizing its performance under such conditions, as oxidation resistance has a direct impact on the longevity and structural integrity of the material in demanding operating environments [13,14]. The oxidation properties of 316L steel produced by conventional methods have been extensively investigated in several articles [15,16]. These studies have provided important insights into the oxidation behavior of steel at elevated temperatures. For example, it has been observed that the oxidation of 316L steel follows the parabolic relationship up to approximately 700 °C. Beyond this temperature threshold, the steel deviates from this equation and normally exhibits a non-compliance with the parabolic evolution [15,16]. Nevertheless, Buscail et al. [17]

* Corresponding author.
E-mail address: M.hadi@iut.ac.ir (M. Hadi).

https://doi.org/10.1016/j.jmrt.2024.06.229
Received 3 May 2024; Received in revised form 18 June 2024; Accepted 29 June 2024
Available online 30 June 2024

reported that at higher temperatures such as 900 °C, the parabolic behavior has still observed for the oxidation of 316L steel. From another perspective, the composition of the oxide layer on the surface of 316L steel has been reported differently in various research studies. In some reports the Cr_2O_3 compound has been proposed as the primary constituent of the oxide layer with the presence of manganese-chromium spinel in the form of Mn_2CrO_4 [13] or in the form of $Mn_{1.5}Cr_{1.5}O_4$ [17,18] in the structure, while in other research the presence of Fe_2O_3 alongside Cr_2O_3 has been suggested as the main phases [19]. In addition, there are research studies that discuss the formation of CrO_3 phase or complex compounds such as Fe_2CrO_4 within the oxide layer of 316L steel [16].

The variation of publish research on the oxidation behavior of 316L steel, particularly when considering potential differences due to SLM production, underlines the importance of this issue. It is well known that oxidation in alloys produced by additive manufacturing has its own unique characteristics [20]. Despite the extensive studies on the various properties of SLM produced 316L steel, there has been a notable lack of published information on its oxidation resistance. Siri et al. investigated the oxidation behavior of 316L steel under both SLM and wrought conditions. They stated that the oxidation resistance of the SLM alloy was superior to that of the wrought alloy in the temperature range of 700–1000 °C. They found that the oxidation curves for SLM followed the parabolic equation at all temperatures, whereas the wrought sample showed a linear law above 800 °C [21,22]. In this research, the authors also highlighted discrepancies in reports on the oxidation behavior of 316L steel. They noted that their results contradicted those published in the Benafia et al. [23] report, particularly in the temperature range of 650–750 °C·In another article, Dudziak et al. [24] compared the oxidation behavior of 316L steel between additive manufacturing and conventional methods, revealing fundamental differences from the aforementioned research. This study reported that the composition of the oxide layer in the SLM alloy becomes enriched with iron oxide as the temperature increases up to 900 °C [24]. It is clear, therefore, that there is no consensus among the few published articles on the oxidation of 316L steel produced by the SLM process. The varying results underline the complexity of this phenomenon and highlight the need for further research to elucidate the underlying factors influencing the oxidation behavior of SLM produced components.

The remarkable aspect of parts produced by SLM is the significant microstructural variations, including grain size, inherent in the wrought state. These variations can directly affect the oxidation resistance. The effect of microstructure on the oxidation behavior has been the subject of several studies and reports in other alloys [25–27]. Contrary to the mentioned studies which report an increase in oxidation resistance of 316L steel compared to its wrought state [22,24], there are studies which show that reducing grain size and increasing the number of grain boundaries actually reduces oxidation resistance [28,29]. Therefore, given the well-established fact that SLM alloys exhibit small grain sizes in the molten pool due to their rapid solidification rate [30–32], coupled with the confirmed high stability of these grains at elevated temperatures in 316L steel [33], there is a compelling need for further research. It seems imperative to compare the results of oxidation in SLM produced components with those in wrought counterparts. Also, potential differences in the initial composition of 316L steel produced by SLM and conventional methods have not been considered in previous published research. Due to the different production conditions, particularly the high cooling rate inherent in SLM, small differences in the composition of the primary powder are typically accounted for in the SLM process. These variations have the potential to significantly affect the oxidation behavior. Therefore, a comprehensive consideration of such compositional variations is crucial for a thorough understanding of the oxidation characteristics. Furthermore, a comprehensive elemental analysis of the oxide layer and a structural study of the oxide scale to identify the phases present at different temperatures are additional requisites that have been overlooked in the limited published literature on the oxidation of 316L steel produced by SLM. However, these investigations are imperative for a thorough understanding of the oxidation process and its implications.

In this research, the oxidation behavior of 316L steel produced by SLM and wrought, within the temperature range of 600 °C–900 °C, has been thoroughly investigated. Complementing previous research efforts, a comprehensive comparison of the primary chemical composition, detailed elemental analysis of the oxide scale formed on the surface at different temperatures, and structural investigation of the phases within the oxide scale were carried out. This holistic approach provides a more comprehensive understanding of the oxidation characteristics of SLM produced 316L steel compared to the wrought counterpart.

2. 2- Experimental details

In this study, 316L steel was meticulously prepared and analyzed using two different production methods. The first involved the use of as-received steel in a wrought condition, prepared in accordance with the ASTM-A240 standard. The wrought 316L steel was then carefully compared with the 316L steel produced using the selective laser melting (SLM) process. Rectangular cube-shaped parts with dimensions of 100 × 100 × 500 mm were produced using gas atomized 316L powder (<65 μm) with a particle size distribution of d10 equal to 5.7 μm as the starting powder with a layer thickness of 30 μm. The process was carried out on a Noura M100P machine with a maximum power of 300 W. The number of slices during the build was 345 and a declining sequential pattern was used for the laser scanning pattern. Additive manufacturing was performed on a platform size (D-Z) of 124*150 mm. Quantitative analysis was conducted to ascertain the composition of elements within the alloy, utilizing an ARL 3560 Optical Emission Spectrometer (OES) device. To examine the metallographic structure of the samples, the surface of the test samples was examined according to the guidelines of ASTM standards E3 and E407. As the morphology was not clearly visible with traditional etching solutions, the electro-etching method was used to improve visibility and obtain accurate images. The electro-etching process is carried out in a 40% NaOH solution at a voltage of about 2 V for 15 s at room temperature. Differential scanning calorimetry (DSC) and thermogravimetric analysis (TG) tests were conducted on the samples using an SDT Q600 model device. The tests were performed at a heating rate of 5 °C/min from 25 °C to 1000 °C under air atmosphere. To prepare the samples for the isothermal oxidation test, discs of 10 × 10 mm and 1 mm thick were produced by electrical discharge wire cutting. Mass changes, including oxide spalls, were measured with an AND balance to an accuracy of 0.1 mg. The isothermal oxidation mass-gain measurements were conducted at temperatures ranging from 600 °C to 900 °C for a duration of 100 h. To ensure repeatability, each test was performed three times. The mass gain data were fitted with the parabolic equation of oxidation to calculate the parabolic rate constant (k_p) using Sigmaplot software. The oxidation layers were carefully examined by scanning electron microscopy (SEM) using a MIRA TE-Scan instrument equipped with energy dispersive X-ray spectroscopy (EDS). For structural analysis of the oxide scale, grazing incidence X-ray diffraction (GIXRD) was performed using an X-ray diffractometer (XRD). The phase composition and crystal structures of both SLM and wrought samples were investigated at room temperature using X-ray powder diffraction measurements. X-ray powder diffraction data were acquired under ambient conditions using a high-resolution laboratory X-ray powder diffractometer (Bruker D8 ADVANCE) equipped with $CuK_\alpha 1$ radiation from a primary Ge (111)-Johannson type monochromator and a Våntag-1 position sensitive detector (PSD) arranged in Debye-Scherrer geometry. Data acquisition was performed continuously in steps of 0.008 from 5 to 90 (2 theta) at a rate of 0.03° min^{-1}. Qualitative phase analysis was performed using the PDF-2 database (ICDD, 2016) in conjunction with the X'pert High Score program for phase identification. Rietveld refinement was performed using the TOPAS 4–2 program.

3. 3- Results and discussions

3.1. 3-1 initial composition and microstructure

To compare the chemical composition of the SLM and wrought alloys, the OES analysis is shown in Table 1. The results show a lower concentration of carbon, and a higher proportion of phosphorus and sulfur can be observed in the SLM sample. Although OES cannot determine these elements with precision, since the results were obtained by repeated tests and averaging 4 tests with a standard deviation of less than 5%, if we accept the difference in the direction obtained, it can be interpreted as follows. According to the research of Andreata et al. [34], the elevated levels of phosphorus and sulfur in the SLM samples have a minimal effect on their electrochemical behavior compared to the wrought samples. In addition, the lower C concentration is selected for proper phase stability due to the rapid cooling rate promoted by the laser beam of the SLM process. It is important to note that this discrepancy results in the carbon content of the wrought alloy being almost three times higher than that of the SLM alloy. While some studies have demonstrated the detrimental effect of carbon on the oxidation properties of chromium stainless steels [35], it is noteworthy that other studies have suggested the opposite [36]. In particular, some studies suggest that a slight increase in interstitial carbon content can actually improve the oxidation resistance of stainless steels [36]. It should be noted that with this method of analysis it is not possible to determine the exact difference in the amount of carbon present. The comparison of the two compositions also shows that the amount of manganese in the SLM sample is slightly lower than in the wrought sample. Previous articles have consistently reported the significant impact of manganese on the oxidation properties of stainless steels [28]. In particular, the presence of manganese is noted to facilitate the formation of the protective oxide layer, thereby increasing the material's resistance to oxidation [24]. While the difference in molybdenum content may seem small according to Table 1, previous studies indicate that variations in chromium and nickel content can influence oxidation properties. Chromium stands out as the most important element influencing the oxidation resistance of stainless steels, and there is widespread agreement that it plays a crucial role in the oxidation properties [15–18]. Consequently, even a small reduction in the amount of chromium present in the SLM alloy can potentially affect its oxidation properties. The crucial aspect highlighted in the comparison of the composition of the two samples shown in Table 1 is the higher concentrations of the elements nickel, manganese, and chromium in the wrought sample. These elements are known to have a positive effect on oxidation resistance. It's worth noting, however, that the lower levels of these elements in the SLM sample are offset by an increased amount of the base element, iron, in the SLM sample. This finding is particularly significant in selective oxidation processes, where the competition between chromium and iron to form an oxide layer on the surface plays a pivotal role.

These differences can indeed have a significant impact on the oxidation properties and have not been adequately emphasized in previous published articles comparing the SLM and wrought oxidation [21–24]. Some of the inconsistencies observed in previous research, as discussed in the Introduction section, can be attributed to differences in initial composition. Recognizing these differences is crucial as they can profoundly affect the oxidation behavior of the alloy. Understanding the elemental factors that influence oxidation properties can guide the preparation of primary powders for the SLM process, ultimately improving the alloy's resistance to oxidation.

Fig. 1 shows the microstructure images of the as-built SLM alloy (Fig. 1-(a) and (b)) and the wrought alloy (Fig. 1-(c) and (d)) at two magnifications. The microstructure of the SLM alloy is characterized by the presence of melt pools that continuously form on top of each other. In the microstructure of the SLM alloy, the first boundary of significant energy that can be seen in etching is the boundary of the melt pools formed during manufacture. These regions are created by the solidification of molten droplets when the laser beam is positioned at any point on the powder bed and then passed through it during the SLM process [37]. However, it is important to note that in addition to the prominent boundaries with significant energy that are visible in the etching, there are secondary boundaries within the melt pools, indicated by arrows in Fig. 1-(b). These boundaries, which are difficult to detect in the resolution of the light microscope due to their small size, are grain boundaries created by the rapid solidification rate of the alloy during the SLM process [38]. SEM images were also used to further investigate the microstructure containing these small grains in the SLM sample. Fig. 1 (c) and (d) in two different magnifications clearly show the formation of these small grains within the melt pools. It can be seen that a nanoscale structure has formed in the SLM alloy. In this study, the effects of melt pool boundaries and grain boundaries are investigated and evaluated as part of the oxidation process investigations. In addition, voids can be seen in the microstructure of the SLM alloy. These voids, which often have a round and spherical appearance, are pinholes of gas porosity that were present in the primary powder particles used for SLM. Previous research has shown that such voids can form in SLM parts due to gases dissolved in the initial powder due to the gas atomization process [39].

On the other hand, within the microstructure of the wrought alloy (Fig. 1-(e) and (f)), at two different magnifications, the fine-grained microstructure consists of twinned grains resulting from the deformation process. Previous work has shown that twin boundaries can form in the microstructure of austenitic steels during hot working and annealing. Since 316L steels are typically processed at high temperatures, the grain microstructure does not have a strong orientation and a relatively equiaxed grain structure is usually produced. Overall, it can be said that the microstructural comparison of the two alloys clearly shows the primary difference. As it will be discussed later the oxidation behavior between the SLM alloy, and the wrought alloy can be understood based on these microstructural differences. The magnification of figure (e) is 200 times and corresponds to the magnification of figure (b) in the SLM alloy, and therefore the contrast between these two images shows that the average dimension of the melt pools in the SLM alloy is significantly higher than the grain dimensions produced within the alloy. However, the point to be highlighted here is that inside the melt pools, the grain size of the SLM alloy is finer than that of the wrought alloy. Therefore, from the boundaries created in the microstructure, which we know from previous studies can be oxygen penetration paths [29], there are two approaches including melt pools and grains inside these pools. According to the first view, the melt pools are larger than the grain dimensions of the wrought alloy and thus there are fewer boundaries in the SLM alloy from this perspective. On the other hand, according to the second viewpoint, the grains within the melt pools in the SLM alloy are more refined than in the wrought alloy and therefore the grain boundary area in the SLM alloy is larger than in the wrought alloy. In other words, the cellular and nanoscale structure formed in the SLM alloy, as seen in the images of Fig. 1(d) and (e), provides more pathways for oxygen to penetrate the SLM alloy, which can directly affect the oxidation

Table 1
Chemical compositions obtained from the wrought and SLM samples by optical emission spectrometer.

Element	C	Si	Mn	S	P	Cr	Mo	Ni	Cu	Fe
Wrought	0.03	0.53	1.79	0.005	0.008	16.94	2.79	12.69	0.03	Balanced
SLM	0.012	0.59	1.30	0.012	0.014	16.60	3.00	12.10	0.03	Balanced
ASTM-A240	0 - 0.03	0 - 1	1.25 - 2	0 - 0.03	0 - 0.04	16 - 18	2 - 3	10 - 14	0 - 1	Balanced

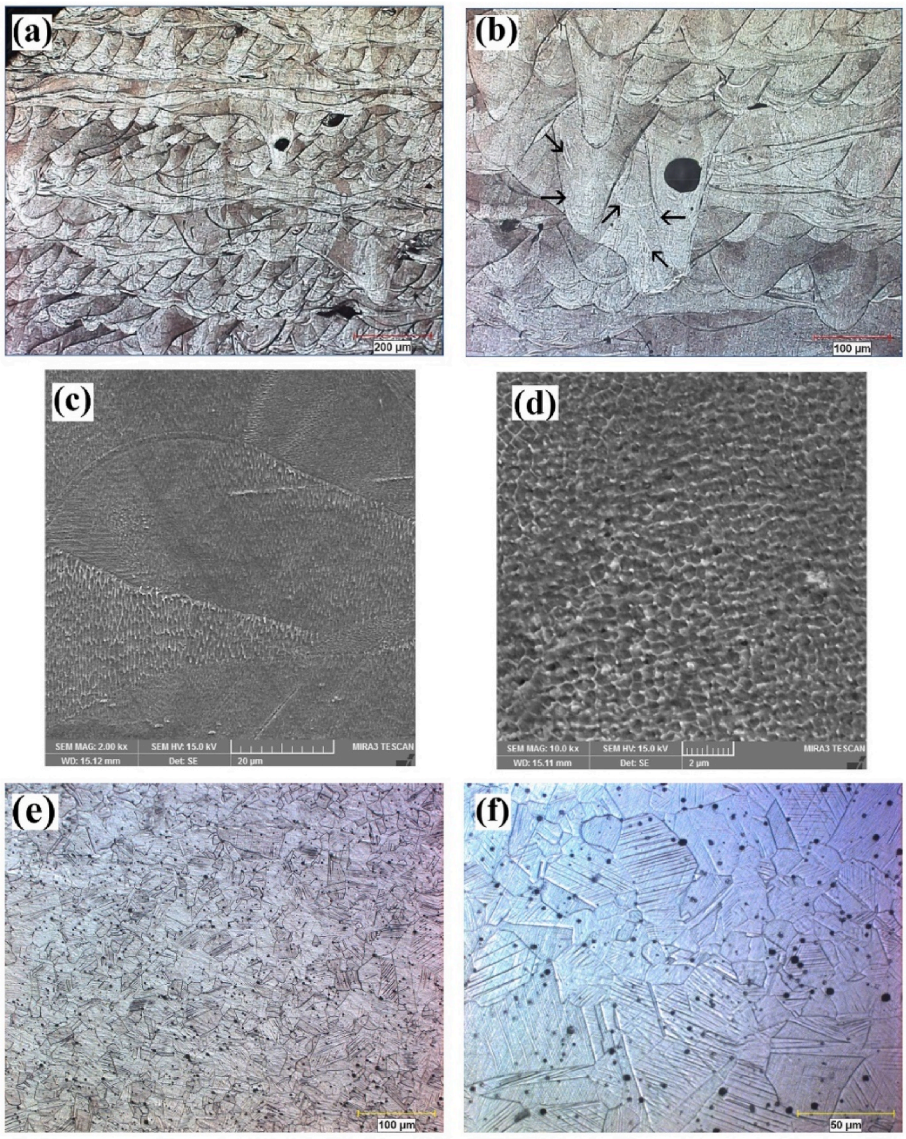

Fig. 1. Optical microscopy images of the SLM alloy (a and b) together with SEM images of fine grains in the melt pool of this specimen (c and d) and optical microscopy images of the wrought alloy (e and f).

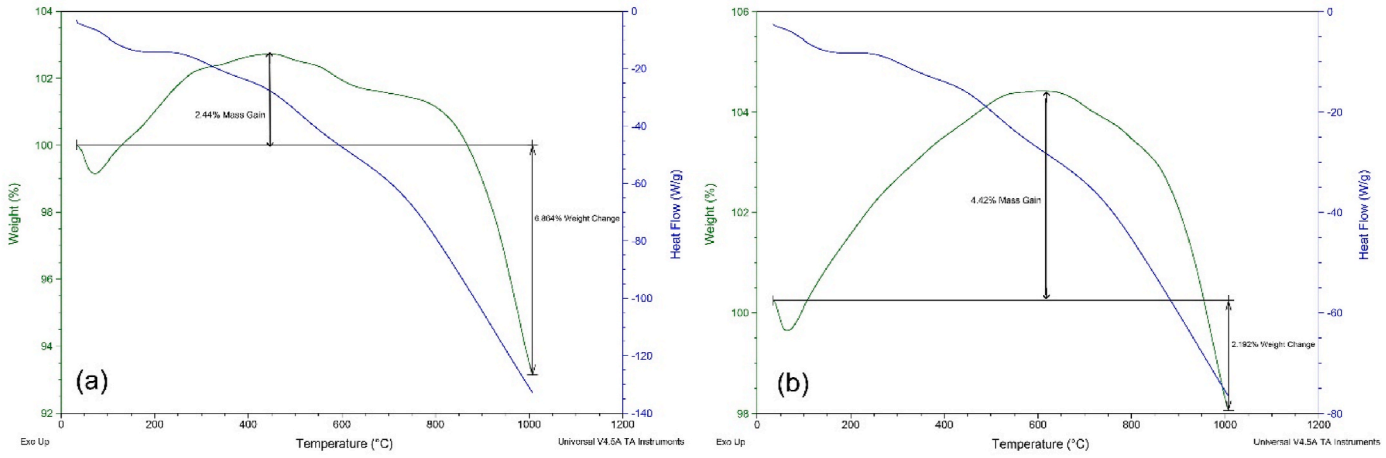

Fig. 2. Differential Scanning Calorimetry (DSC) and Thermogravimetric Analysis (TGA) of the alloy in blue and green color curves respectively in the (a) SLM and (b) wrought samples. (For interpretation of the references to color in this figure legend, the reader is referred to the Web version of this article.)

resistance. Our results show that this analysis is more appropriate to interpret the observed differences in oxidation resistance between the two alloys as follows. It is noteworthy that the intensity of the microstructural changes over time in the SLM and wrought samples was investigated and the results showed that the microstructural changes in both samples were completely negligible.

3.2. 3-2- oxidation behavior

The results of the non-isothermal oxidation test based on thermogravimetric analysis (TGA) and differential scanning calorimetry (DSC) in air atmosphere for SLM and wrought samples are shown in Fig. 2. These graphs show that the thermal behavior of the two alloys (blue DSC curves) is completely equivalent, suggesting that the change in manufacturing process from traditional casting to SLM process has not caused any change in the phase stability and phase transitions of the alloy. The reason for the similarity can be attributed to the fact that although the high cooling rate during SLM completely affects the microstructure of the alloy, it does not influence the phase stability of the 316L alloy, which is an austenitic steel. In fact, the presence of austenite stabilizing alloying elements in 316L steel results in the formation of a stable austenite phase within the structure, regardless of the significant difference in cooling speed between the two manufacturing techniques. Fig. 2 also shows the weight variations of the two alloys as the temperature rises to 1000 °C in the green-colored curves. As can be seen, the weight gain of the wrought alloy was greater than that of the SLM alloy. According to the data, the amount of mass gain during the temperature increase in the SLM alloy was 2.44% of the initial weight at the beginning of the test, while in the wrought alloy this figure was 4.42% of the initial weight. This difference clearly shows that the SLM alloy has a higher resistance to oxidation than the wrought alloy in the case of non-isothermal testing (heating speed 5 °C/min). The subsequent decrease in weight gain after the maximum mass increase is reached may be due to the extraction of outgassed items or gases resulting from oxidation reactions. Previous research has shown that when Fe, rather than chromium, begins to oxidize on the surface of stainless steel, carbon is also removed through interaction with oxygen in the form of CO, which can lead to a reduction in mass [40]. In other words, if there is a loss of mass due to the emission of CO gas as an indicator of greater oxidation of the Fe element compared to Cr, we can see that in the SLM alloy, where the weight loss was greater, the rate of iron oxidation would perhaps be more dominant than in the wrought alloy. This idea will be used in the following discussions to compare the long-term oxidation capabilities of the two alloys.

To understand the result, it can be stated that in the wrought form of 316L steel, the microstructure is made up of small grains and, consequently, the number of grain boundaries is extensive. The notion that the grain boundary in austenitic stainless steels can act as a penetration path has been raised in previous research, including that of Kim et al. [25]. However, as mentioned above, although the number of boundaries within the melt pools of the SLM alloy is lower (as these pools are coarse), the grains enclosed within the pools are extremely small. Consequently, it appears that in the non-isothermal oxidation test, which is performed in a short time (about 200 min), the greater number of grain boundaries in the wrought alloy, as opposed to the intense boundaries of the melt pools, may be the reason for more oxygen entering through the surface, which ultimately results in the higher oxidation of the wrought alloy. Furthermore, the TG results show that the total mass gain of the wrought alloy is greater than that of the SLM alloy, but at the same time the weight loss rate at high temperatures is less than that of the SLM alloy. Putting these two results together, and considering that previous studies have shown that the main cause of weight loss at high temperatures in steels is the combination of oxygen with carbon, and that this phenomenon occurs when iron oxidation is dominant, it can be concluded that the higher mass gain observed in the wrought alloy may be caused by the formation of an oxide layer with less iron and more chromium (discussed below).

Fig. 3 summarizes the mass gain of specimens after isothermal exposure. As can be seen from the figure, the initial temperature studied was 600 °C, where the amount of oxidation was low and the oxidation behavior of the two alloys, whether SLM or wrought, was almost identical particularly in the first hours of the test. However, in more prolonged periods, the SLM produced specimen showed greater weight gain than the wrought specimen. As this observation seems to contradict the result of the non-isothermal oxidation test, where the mass gain of the wrought sample was much higher, a more thorough investigation is required. From the graphs of the two alloys at 600 °C, the progression of oxidation within the initial periods is relatively similar and in the longer periods the wrought sample showed less oxidation. Admittedly, the difference between the two samples at 600 °C was not distinctive, even in the biggest spots. In addition, the amount of oxidation and mass gain is also quite small. When the temperature was increased to 700 °C, a similar tendency to the 600 °C test conditions was observed, and the change process and rate of mass increase were not significantly different from the 600 °C curve, therefore the 700 °C is not shown in Fig. 3.

The oxidation results at the temperature of 800 °C show a significant difference in the amount of oxidation between the SLM and wrought samples. This difference in the trend of the curves has two stages. In the first stage and early times, the oxidation curve of the SLM alloy is significantly lower than that of the wrought alloy sample. By approximately 45 h, the amount of mass gain in both samples is equal, and as time progresses, the mass gain in the SLM sample tends to be higher than in the wrought sample, and the graph becomes steeper. In the wrought sample at this temperature, the mass variations over time have reached a considerable consistency and the intensity of the mass increase is significantly lower compared to the SLM case. The reproducibility of these results, as mentioned in the experimental details section, has been confirmed by several tests. This finding shows that the oxidation behavior of 316L steel consists of intricate details which require intensive investigation to analyze and interpret, including structural analysis (Grazing) as well as microstructural and elemental chemical composition studies (SEM, EDS). The point that can be concluded so far is that it appears that in the short times the main paths of oxygen diffusion were the boundaries of the melt pools in the SLM alloy and the boundaries of the grains in the wrought alloy, and because the grain boundary of the wrought alloy (which is a relatively fine-grained alloy) is more than the boundary of the melt pools in the SLM alloy, the amount of oxidation in

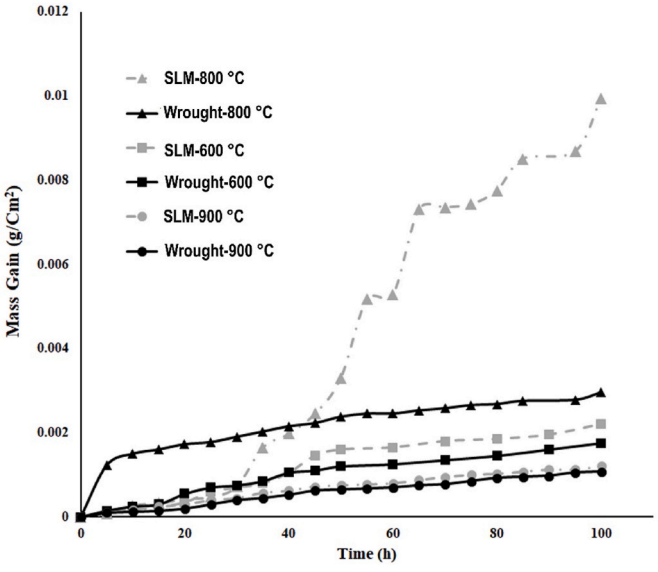

Fig. 3. Results of isothermal oxidation tests at different temperatures for the 316L steel in SLM and wrought forms.

the wrought alloy was greater. This part of the curves concurs with the results of the TG experiment where the oxidation rate of the wrought alloy was higher (see Fig. 2). However, the point is that over longer periods of time, with the likelihood of altering the constitution of the oxide layer, the relative oxidation habits of the two alloys evolve and the curve of the wrought alloy becomes like that of the alloy that formed the passive layer. This is consistent with the result of the TG analysis which showed that the weight loss of the wrought sample was less, indicating that the decarburization and release of CO gas and the oxidation of iron (compared to chromium) in the oxide layer were less in this alloy.

It is interesting to note that by raising the temperature to 900 °C, the oxidation behavior of the SLM alloy and the wrought alloy are very close, and the marked difference in oxidation behavior observed at 800 °C is absent. In addition, the numerical value of the mass gain at 900 °C on the vertical axis is reduced to values much lower than at 800 °C. The results show that the total mass gain at 800 °C after 100 h is higher for both samples, especially for the SLM sample, which is approximately 1.7 times higher than 600 °C and 2.8 times higher than 900 °C.

The outcome of fitting the results obtained at different temperatures with the parabolic equation $\left(\frac{\Delta m}{s}\right)^2 = k_p t$ is given in Table 2, where Δm/s is the mass gain per area, k_p is the oxidation coefficient, and t is time), which is a common equation for the oxidation of metal alloys controlled by the diffusion mechanism of their oxidation [41–43]. The results obtained show a higher k_p value for the SLM sample compared to the wrought at all temperatures, and a higher value at 800 °C compared to the other temperatures. The first result can be attributed to the smaller grains formed within the melt pools in the SLM alloy. Studies show that the diffusion coefficient of oxygen in grain boundaries can be tens of times greater than that of bulk diffusion [28]. The microstructural study revealed that the high solidification rate results in fine grains in SLM alloys. In fact, the cellular and fine-grained microstructure with a size in the nanometer range of the SLM alloy revealed by the SEM results (Fig. 1-(d)) may increase the possibility of oxygen penetration and further expose the alloy to oxidation. Another aspect that may be effective in increasing the oxidation rate of the SLM alloy, in addition to being fine-grained, is the lower amount of manganese element in the SLM alloy compared to the wrought alloy. The results of the compositional analysis of the two alloys in Table 1 show that the manganese element in the SLM alloy is lower than that of the wrought alloy. Studies on grain boundary oxidation in steels have shown that increasing the amount of manganese has a direct role in reducing the grain boundary oxidation [28]. In addition to manganese, less chromium, and nickel in the composition of the SLM alloy, which was discussed in the explanation of Table 1, can also be effective in the difference in the oxidation behavior. To interpret the second finding revealed by the comparison of the k_p results, i.e. the higher oxidation rate at 800 °C compared to other temperatures, the analysis of the oxide layer should be considered, which will be discussed in detail in the rest of this article.

It is worth noting that the degree of agreement of the behavior of the changes in weight gain with time can be measured by the value of R^2. The closer this value is to 1, the better the agreement between the oxidation results and the above equation. The value of R^2 for the SLM sample at 800 °C is significantly lower than the other conditions and shows a weak fit to the above equation. The reasons for this discrepancy are, on one hand, the dependence of the oxidation rate on the spallation rate (which, will see in the following section, was very significant in the SLM sample at 800 °C) and, on the other hand, the presence of cracks and holes in the oxide layer, which has reduced compliance with the equation for interpreting the process with diffusion. Non-compliance with parabolic oxidation kinetics has been reported for 316L steel in previous investigations [16]. Therefore, it seems that the comparison and study of the oxidation process in the SLM and wrought conditions, requires the investigation of factors affecting it, including the constitution of the oxide layer and the porosity/compactness of the layer produced, which will be addressed in section 3-3.

Table 2
The values obtained by fitting the oxidation results in different samples and temperatures with the parabolic equation.

Temperature (°C)	Sample	k_p	R-squared
600	SLM	$5*10^{-8}$	0.95
	Wrought	$2.5*10^{-8}$	0.98
800	SLM	$1*10^{-6}$	0.86
	Wrought	$1*10^{-7}$	0.98
900	SLM	$1.25*10^{-8}$	0.98
	Wrought	$1*10^{-8}$	0.97

3.3. 3-3- oxidized morphology and structure

The SEM image of the top surface of the oxide scale after 100 h of oxidation at 600 °C for the SLM alloy is presented in Fig. 4. As can be seen in the figure, several regions with different morphologies in the surface oxide layer have been identified by the secondary electron detector, named from A to D. The composition of the regions A to D that were examined by the EDS is also depicted in the figure. The elemental analysis of the specified regions revealed that, despite the different appearance of these regions in the oxide layer, labelled A to D, they all contain the elements Fe, Cr, O and a limited amount of Ni, Mo, Mn. This indicates that the oxide phases of iron have taken the lead in the oxide layer of the SLM alloy. In the case of areas C, it can be observed that they are similar in composition to the matrix; however, carbon has also been absorbed due to surface contamination, resulting in not being a discrete part of the oxide scale. Furthermore, the difference in the amount of carbon determined using EDS is not certain. Therefore, it can be assumed that these regions have the same composition. It is also worth noting that the areas marked with the letter D, which form hillocks on the surface of the oxide scale, contain more iron and oxygen, while the amount of chromium and other alloying elements is reduced. Fig. 4-c shows another example of the formation of these hills at a point far from where Fig. 4-a was taken, at different magnifications. The EDS study of these hills also showed that they have a very similar composition to region D in Fig. 4-a. Considering the reproducibility of this result in other parts of the sample where the height of the oxide surface was greater, it appears that the formation of these hills on the outer surface of the oxide layer is directly related to the composition of the oxide produced. In fact, the iron oxide in the oxide scale of the SLM alloy can form hills on the surface and grow in a heterogeneous manner. Another point that can be seen in Fig. 4-c is that the morphology of the background oxide scale is also uniformly distributed over the entire surface, but it is not very dense, and many pores can be seen in it. Interestingly, the formed hills have a less porous morphology than the matrix, as can be seen in the second and third parts of Fig. 4-c. The importance of the formation of these hills in the oxide layer of the SLM alloy is that previous studies have shown that during the oxidation process, the formation of oxide hills with preferential growth over the entire surface of the scale reduces the adhesion of the oxide layer to the surface and causes spallation [41,44].

Fig. 5 shows the SEM images of the upper surface of the wrought sample, which has been oxidized in air at the temperature of 600 °C, taken from two different points. It is clear from this image that the grain boundaries of the wrought microstructure have been retained in the outer oxide layer and this shows that the grain boundaries had different oxidation conditions, which is the reason that they are visible in the SEM after oxidation because they have different heights. Fig. 5-a shows the hill-like regions, which are smaller in volume than the SLM sample but similar in microstructure, at two different magnifications. Other regions where the morphology of the oxide scale and its height are different are shown in Fig. 5-b. Based on this, the analysis of the four areas identified in the oxide layer of the wrought alloy, which have different shapes, are labelled A, B, C, D and placed next to the corresponding pictures. As can

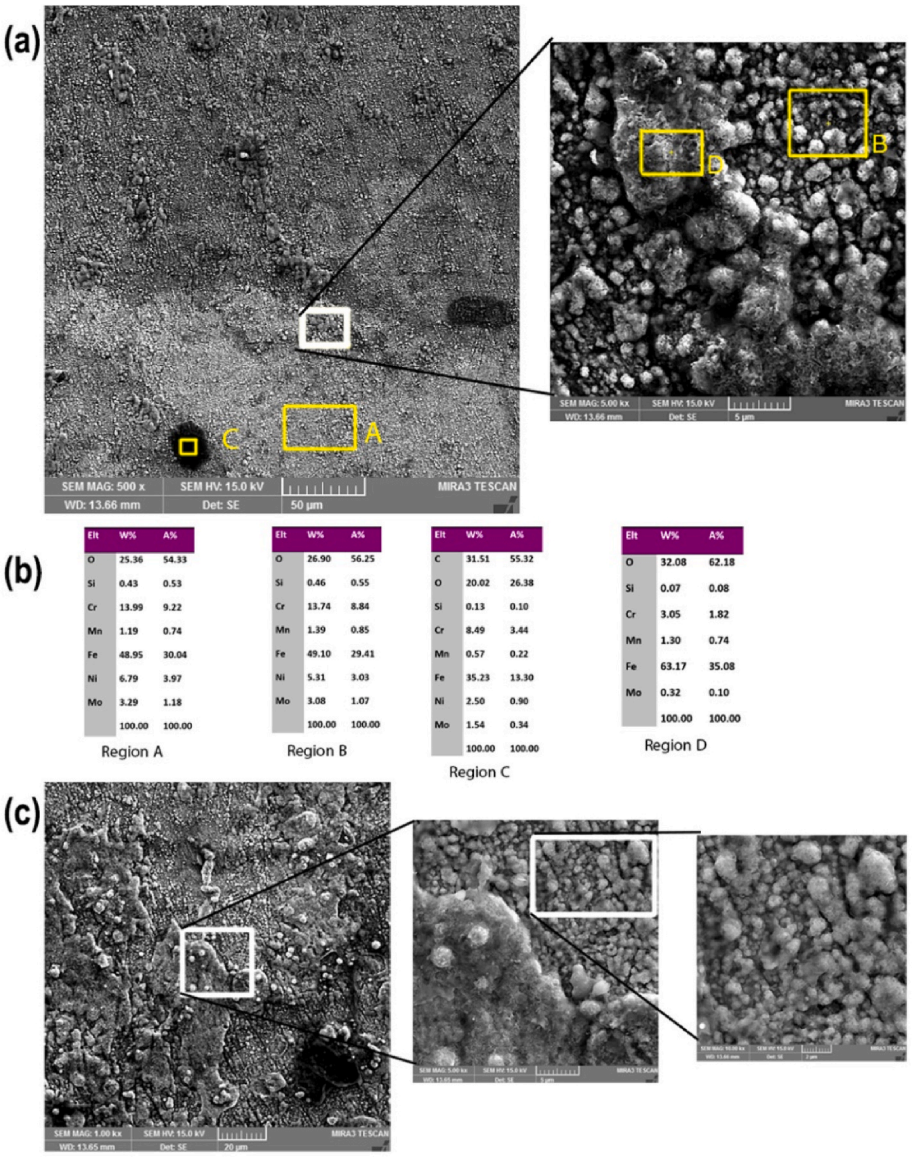

Fig. 4. (a) SEM image of the top surface of the oxide layer of the SLM alloy that was oxidized at 600 °C after 100 h, (b) EDS analysis of the regions marked in part (a), and (c) another SEM image and magnifications from a distant point.

be seen in Fig. 5, the hill-like areas marked A are oxide-rich regions of iron, and comparison of the composition of this region with region D in Fig. 4, associated with the SLM alloy, clearly demonstrates that they have a similar constitution.

The elemental composition of the oxide layer in the wrought alloy, labelled B in Fig. 5, differs from that of the oxide base in the SLM alloy, also labelled B in Fig. 4. Examination of this area, and of the other points of the oxide layer on the wrought sample, reveals that the amount of chromium in the oxide layer was reduced. The elemental analysis of areas A and C in the oxide layer of the part has the same composition and is similar except for a few elements such as Cr. In the areas of the oxide layer of the wrought material marked with the letter D, the combination of iron oxide predominates, but the mixture of oxides of other elements, has also developed, forming a complex mixture of oxides.

To investigate this further, a large area of the outer surface of the oxide layer was analyzed by EDS on two samples, one SLM and one wrought, and the result of such an operation can be seen in Fig. 6-(a) and (b). As can be seen from this figure, the oxide scale of the SLM sample contains Cr, Mo, and Ni elements in addition to iron oxide to a greater extent than the wrought alloy. It is known that chromium oxide forms a more resistant layer on the outside against further oxidation but combining the result of the variation in the composition of the oxide layers (Fig. 6-(a) and (b)) with the result of the mass gains (Fig. 3) shows that this small change in the composition of the oxide layers was not able to reduce the amount of oxidation. The key point in interpreting the apparent contradiction is that at 600 °C the oxidation rate of both samples is almost similar and its numerical value on the vertical axis in Fig. 3 is extremely diminished. In fact, the amount of oxidation on the two specimens is not so great that a small variance in the composition of the oxide layer would result in a difference in the rate of oxidation. In addition, the amount of chromium required to form protective phases on the surface, as we will see in the rest of the article, should be greater than the amount formed in the oxide layer of the SLM sample at 600 °C. In other words, the dissolution of this insignificant number of alloying elements in the oxide layer of the SLM alloy at 600 °C did not act as a barrier to oxygen penetration. In contrast, as can be seen from Figs. 4 and 5, in the oxide layer of the SLM specimen, the preferential growth in the form of a hill is more pronounced and the compactness of the oxide layer is less. In fact, the results show that these factors were more effective at this temperature and caused the oxidation rate in the SLM

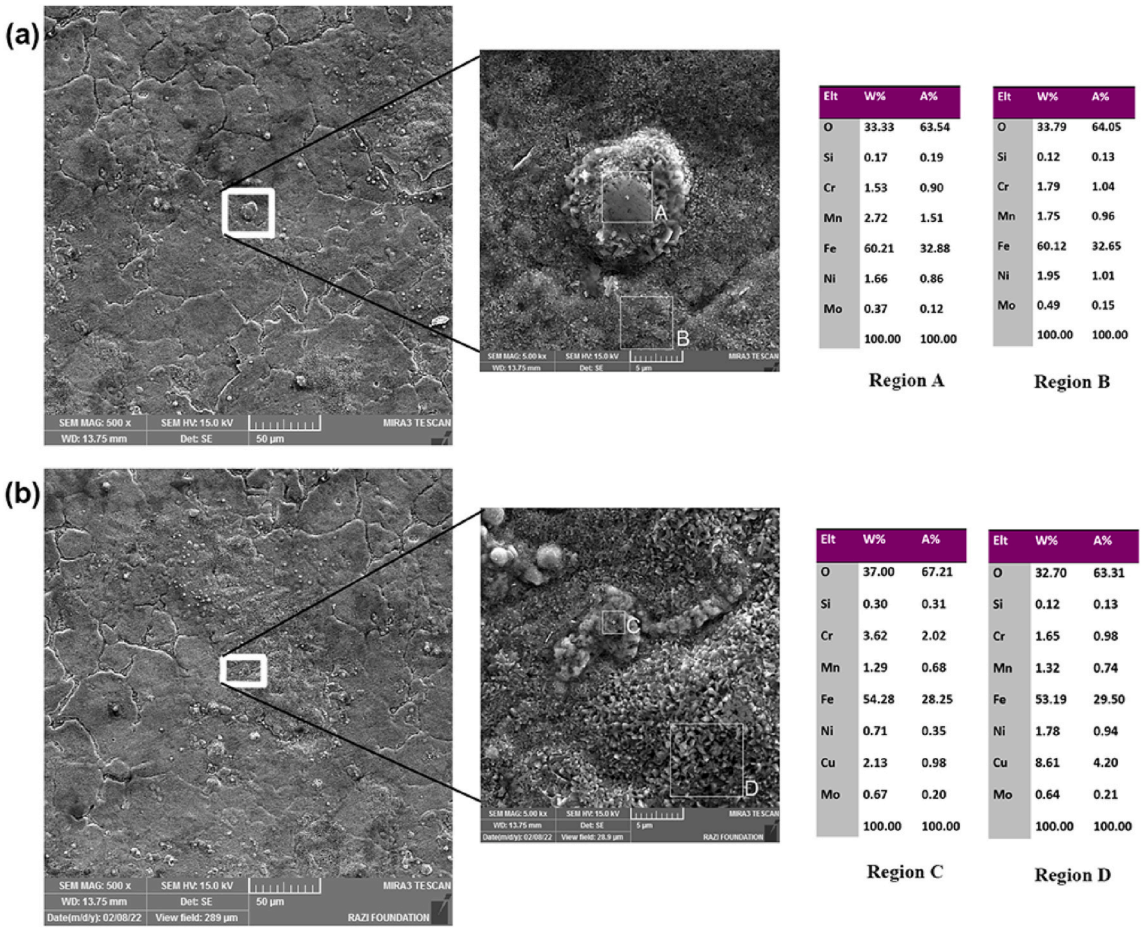

Fig. 5. The SEM images of the top surface of the wrought sample oxidized at 600 °C at two different magnifications (a) and (b) together with the EDS analysis of the marked areas.

alloy to be slightly higher.

However, the results obtained from oxidation at a temperature of 800 °C are of particular importance. At this temperature it is easier to distinguish the difference between the oxidation curve of the SLM sample and the wrought sample, and in both samples the rate of mass increase is higher than at other temperatures (see Fig. 3). Fig. 6-(c) and (d) shows the results of large area EDS analysis of the oxide scale in the SLM and wrought samples oxidized at 800 °C. These pictures show the top view of the oxide surface of two samples analyzed together with the results of the EDS analysis. The images, taken at low magnification, indicate that after 100 h of oxidation, the oxide layer for the SLM sample has partially been detached and the noticeable surface difference is a result of oxide spallation. This was despite the wrought sample having a uniform oxidized surface with much less spalling. This finding is consistent with the results of the oxidation kinetic curves (Fig. 3) and practical observations during the oxidation test. The data indicated that at this temperature, the mass increase (the sum of the oxide layers formed on the sample and the detached oxides) was greater for the SLM sample at 800 °C.

On the other hand, the result of the total elemental analysis of the oxidized surface in Fig. 6-(d) shows that in the wrought alloy there is a high amount of chromium element in the oxide scale. This amount is almost three times as high as the amount observed in the SLM sample shown in Fig. 6-(c). Previous studies have revealed that the presence of chromium in the oxide layer increases oxidation resistance by lowering the diffusion coefficient [21]. The amount of manganese in the oxide layer of the wrought alloy is also significantly higher than that of the SLM alloy. Given the positive role of manganese in increasing oxidation resistance, this change is important. Therefore, the significantly higher amount of chromium and manganese elements in the oxide layer of the wrought sample compared to the SLM sample may be one of the main reasons for the higher oxidation resistance of the wrought sample compared to the SLM sample at a temperature of 800 °C. Comparison of the elemental analysis of the two samples also shows that the amount of Fe in the oxide scale of the wrought sample is significantly lower, in other words it appears that in the wrought sample chromium and manganese have replaced iron in the composition of the oxide layer. It is noteworthy that the amount of chromium in the oxide layer of the wrought sample was significantly higher than the amount of chromium in the SLM sample at a temperature of 600 °C. It seems that this increase in the amount of chromium has enabled this element to play a role in reducing the diffusion coefficient of the oxide layer and to act as a barrier oxide. Another notable difference in the surface elemental analysis of the two alloys is the significant presence of nickel in the oxide scale of the SLM alloy. Manganese is also observed to be more abundant in the oxide scale of the wrought alloy than in the SLM alloy. It has been mentioned that a higher presence of manganese in the composition of the wrought alloy can lead to a higher resistance to oxidation [28]. The sum of these changes in the composition of the oxide scale, particularly the change in the amount of chromium, has resulted in a higher oxidation resistance in the wrought alloy.

Furthermore, Fig. 6-(e) and (f) shows the comparison of the elemental analysis of a relatively large area above the oxide layer of the SLM and wrought alloys at a temperature of 900 °C. The main visible difference in the analysis obtained compared to lower temperatures is the significant increase in the amount of chromium on the surface of the oxide scale. By increasing the amount of chromium, it has been possible to form a uniform oxide layer of chromium oxide which can act as a

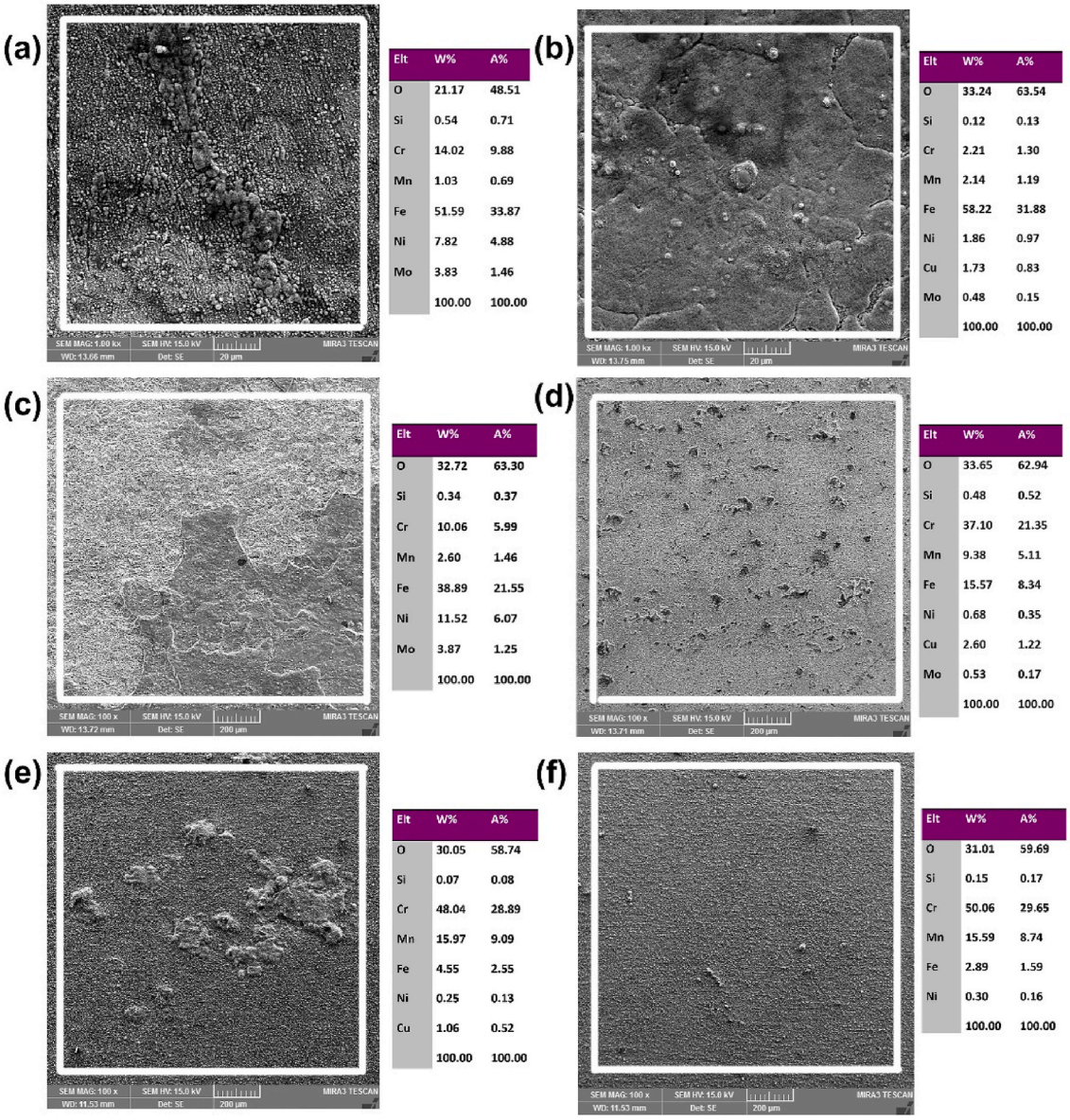

Fig. 6. The EDS analysis of a relatively large area on the surface of the oxide scale for (a) SLM sample at 600 °C, (b) wrought sample at 600 °C, (c) SLM sample at 800 °C, (d) wrought sample at 800 °C, (e) SLM sample at 900 °C, (f) wrought sample at 900 °C.

barrier to further oxidation. As can be seen in Fig. 3, the rate of oxidation at 900 °C is significantly lower than at the other two temperatures. Also of note is the large increase in the amount of manganese in the oxide layer of both alloys at a temperature of 900 °C. In fact, this research clearly confirmed the role of increasing the presence of manganese and decreasing the presence of iron in the oxide layer in reducing the oxidation rate. This shows the importance of paying attention to the amount of manganese in the initial powder materials used for SLM production, especially for applications involving high temperatures.

Fig. 7 illustrates the Rietveld analysis results of the grazing analysis of the outer surfaces of the alloys at different temperatures after 100 h oxidation. The patterns obtained were deciphered using the Rietveld method due to the high background and the location of the peaks was carefully checked using reference cards. Fig. 7-(a) and 7-(b) confirm that at a temperature of 600 °C iron oxide was the predominant phase in both alloys. In addition, a minor peak of chromium oxide is observed in the oxide layer of the SLM alloy, consistent with the EDS results shown in Figs. 4 and 6-(a). However, despite the presence of chromium, the oxidation kinetics (Fig. 3) and surface images of the oxide layer suggest that chromium does not significantly alter the oxidation resistance at this temperature. It is also noteworthy that the oxide layer of both alloys contains the Fe–O phase, indicating a compound with a lower oxygen content compared to conventional iron oxides. This is attributed to the limited penetration of oxygen into the oxide layer due to the slower diffusion rate at this temperature. The contrast between the patterns obtained for the two alloys after oxidation at 800 °C is striking (Fig. 7-(c) and (d)). A key difference is the appearance of a complex oxide phase of iron and manganese in the surface layer of the wrought alloy, which is absent in the oxide layer of the SLM alloy. This is consistent with previous discussions on the role of manganese in mitigating oxidation rates and explains the lower oxidation rate observed in the wrought sample, as shown in Fig. 3. The phase analysis results are also consistent with the compositional results shown in Fig. 6-(c) and 6-(d). At this temperature, while the chromium oxide phase is evident in the patterns of both alloys, its presence is more pronounced in the wrought alloy, in agreement with the results of the EDS analysis. Conversely, within the structure of the oxide layer of the SLM alloy, the Fe–O phase is also detected, with a higher contribution of iron oxide phases compared to the wrought alloy.

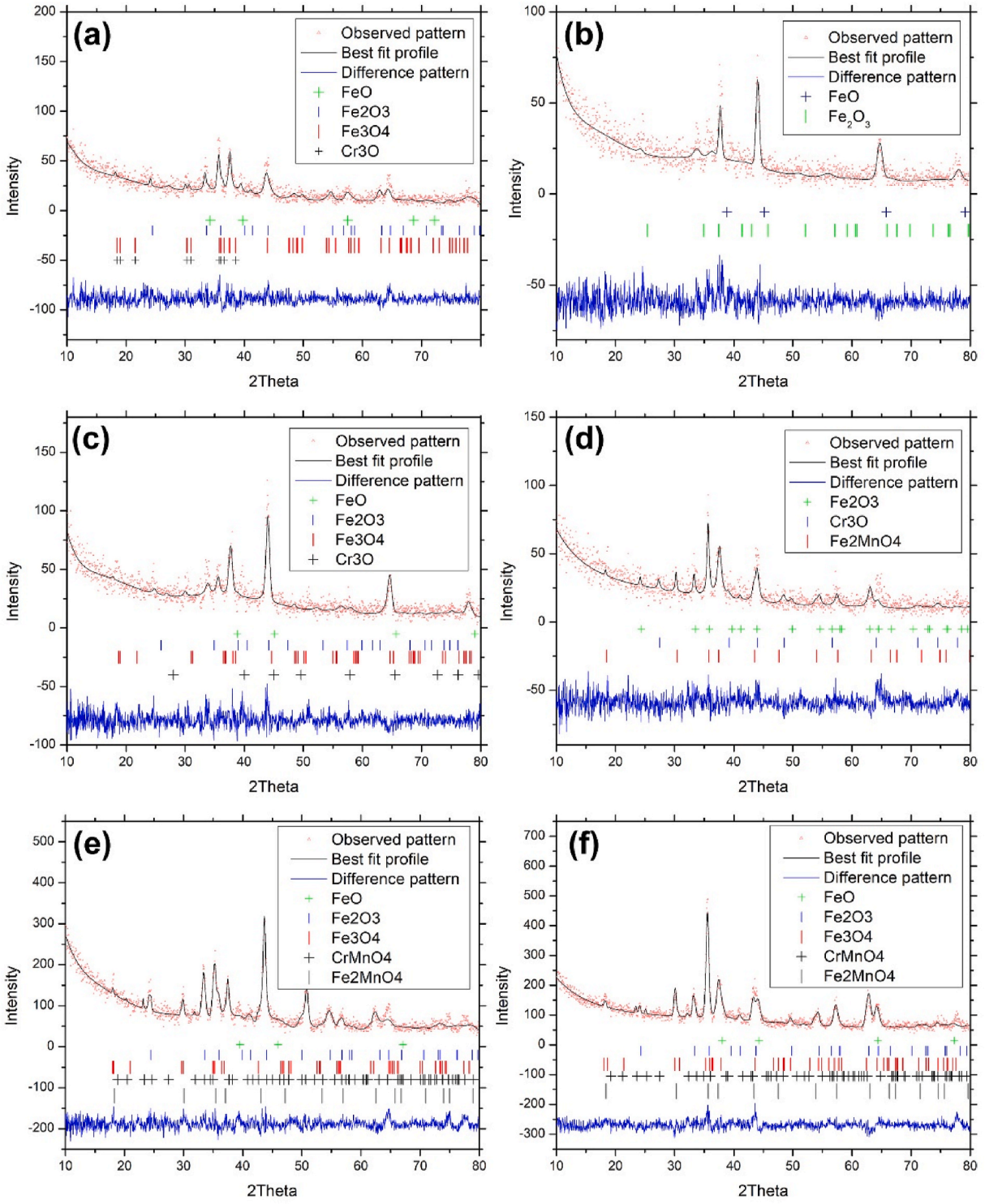

Fig. 7. Grazing incidence X-ray diffraction results with Rietveld refinement for the oxide layers formed after 100 h of isothermal oxidation. (a) SLM sample at 600 °C, (b) wrought sample at 600 °C, (c) SLM sample at 800 °C, (d) wrought sample at 800 °C, (e) SLM sample at 900 °C, (f) wrought sample at 900 °C".

This discrepancy can be attributed to the absence of manganese oxide and the lower amount of chromium oxide in the oxide layer of the SLM alloy, which facilitates higher iron oxide formation. However, as shown in Fig. 7-(e) and (f), the oxide phases formed in the oxide layers of both alloys at 900 °C are almost identical. It is worth noting that the formation of two complex oxide phases containing Cr and Mn, such as $CrMnO_4$ and Fe_2MnO_4, significantly increases the protective ability of the oxide layer. This is in accordance with the results of the oxidation test shown in Fig. 3, which indicates a marked decrease in the oxidation rate at 900 °C. In addition, the prevalence of phases containing chromium and manganese in the oxide layer is consistent with the results of the EDS analysis shown in Fig. 6-(e) and (f). In essence, the results suggest that changes in the oxide phases and the chemical composition of the oxide layer are the main factors contributing to the reduction in the oxidation kinetics at the temperature of 900 °C.

The results of the cross-sectional analysis of the oxide layer of the

samples are also consistent with the interpretation of the oxide surface image. Fig. 8-(a)–(c) show the cross-sectional images of the oxide layer of the SLM alloy at different temperatures. Fig. 8-(d) also shows the image of the oxide layer of the wrought sample at the critical temperature of 800 °C for comparison. From each of the oxidized samples at different temperatures, images were taken from two areas and the EDS analysis obtained from a relatively large area of that oxide layer is displayed alongside. Firstly, it can be seen from this figure that the thickness of the oxide layer at 800 °C was significantly greater than at 600 °C and 900 °C. Meanwhile, at the same temperature of 800 °C, the thickness was higher in the SLM sample than in the wrought sample. These results agree with the results obtained from the oxidation kinetics (Fig. 3). It can also be seen from this figure that the amount of chromium in the sample oxidized at 900 °C (Fig. 7(c)) is significantly higher than the oxide layer of the SLM alloy at 800 °C and 600 °C. A higher amount of manganese is also observed in the cross section of the oxide layer at this temperature. This result confirms that the reduction in the oxidation rate in the alloy is due to the formation of a continuous layer of chromium in the oxide layer and the presence of more manganese in this layer. Comparison of the cross section of the oxide layer of the SLM and wrought alloy at 800 °C also confirms that the amount of chromium in the oxide layer is higher in the wrought sample and has led to a reduction in the thickness of the oxide layer in this sample, but the amount of chromium is not high enough to form a continuous layer of chromium oxide and iron oxide is still dominant. The results of the cross-sectional analysis, including the thickness and composition of the oxide layers, closely match the results of the surface analysis (Fig. 6) and the structural phase analysis (Fig. 7).

The investigation of the oxide/substrate interface in two samples was also carried out using EDS map analysis. Fig. 9 shows the result of this analysis for the critical temperature of 800 °C. The result again confirms that the thickness of the oxide layer in the SLM sample was greater at this temperature.

It can also be seen from this figure that chromium oxide is dominant in the oxide layer immediately after the substrate. This can be seen by comparing the decrease in iron concentration in this area (formation of a dark layer within the green distribution in the Fe map) and the increase in chromium concentration in this area. Comparing the concentration of elements with their color distribution, it can also be seen that in the wrought sample, which had a higher oxidation resistance at this temperature, firstly, the concentration of manganese distribution in the oxide layer of the wrought alloy was higher. Secondly, an increase in the concentration of chromium is again observed on the outer surface of the oxide layer of the worked sample. This can be seen by comparing the chromium distribution in the SLM alloy and the wrought alloy, as the concentration of pink dots in the wrought sample has increased again on the outer surface of the oxide layer in the wrought sample. In the SLM sample, only iron oxide dominates in this region. This result, in agreement with the results examined in Fig. 8, confirms that the increase in the concentration of the two elements chromium and manganese in the oxide layer of the worked alloy was the reason for the higher oxidation resistance in this sample.

Moreover, as can be seen from Fig. 6-(c), the amount of oxide scale spallation in the SLM alloy was much higher. Since the spallation of the oxide scale by increasing the exposure of the substrate to the atmosphere has a direct effect on increasing the oxidation rate, it is important to consider the issue of oxide detachment at 800 °C. Fig. 10 shows images of the detached oxides and their elemental analysis from the SLM and

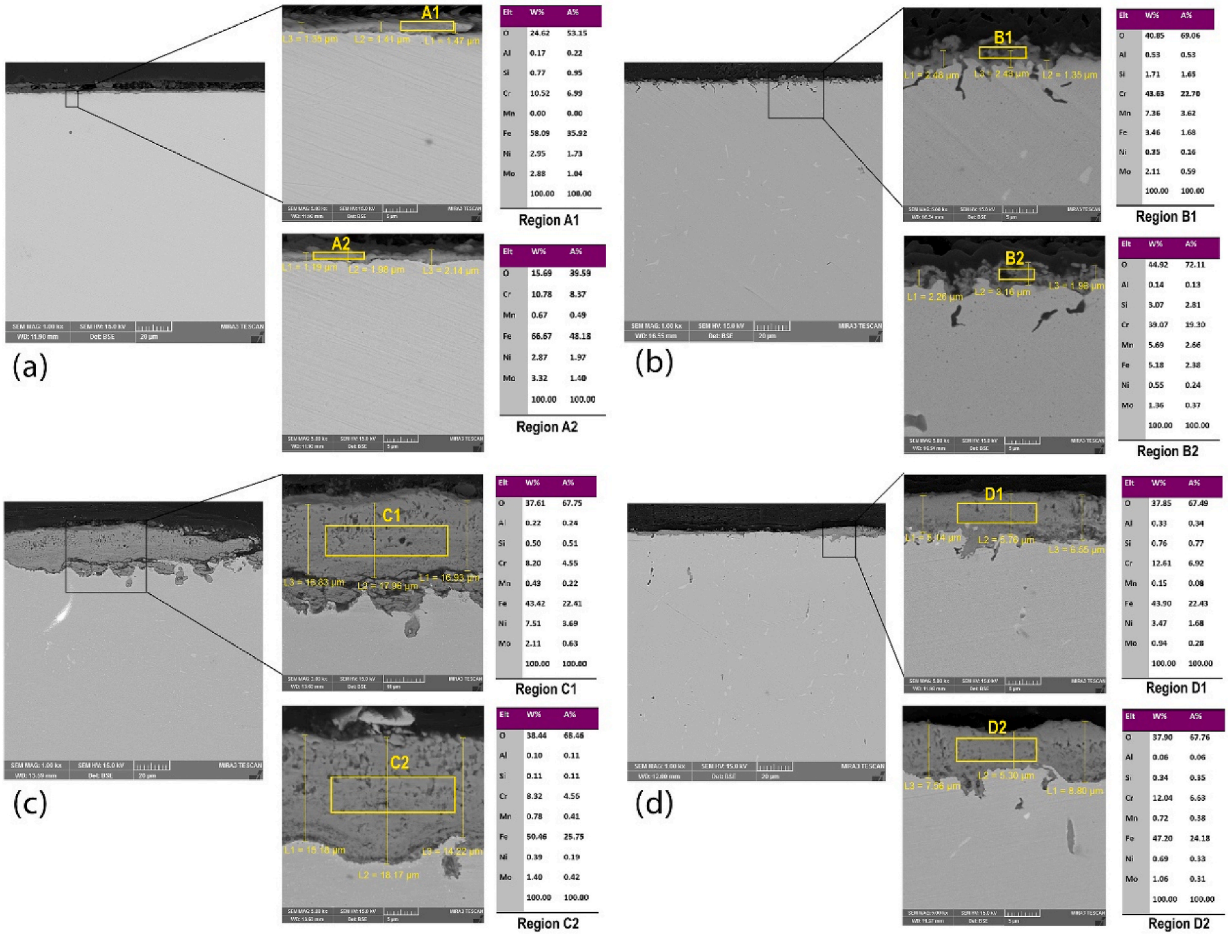

Fig. 8. Cross-sectional images of SLM samples oxidized for (a)100 h at 600 °C, (b) 900 °C and (c) 800 °C and (d) wrought sample oxidized for 100 h at 800 °C.

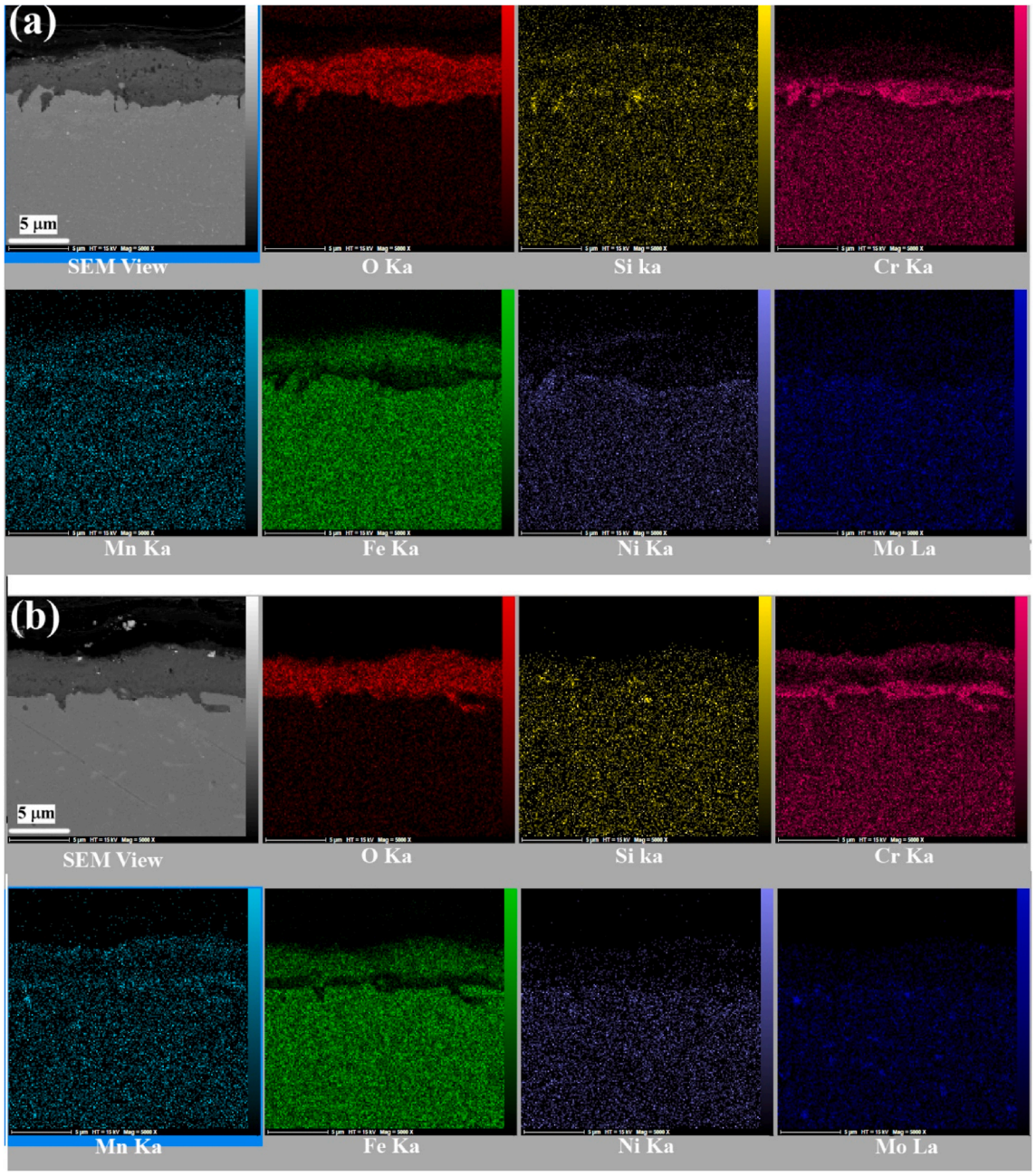

Fig. 9. EDS Map of the oxide/substrate interface zone of SLM (a) and wrought (b) samples oxidized at 800 °C for 100 h.

(a)

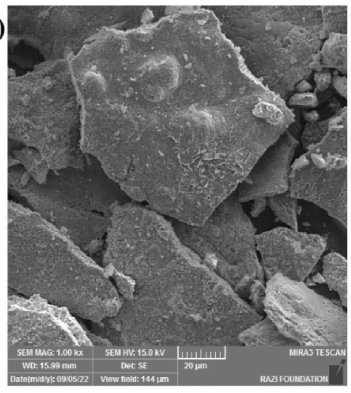

Elt	W%	A%
O	28.46	57.82
Al	0.03	0.03
Si	0.23	0.27
Cr	14.17	8.86
Mn	2.26	1.34
Fe	46.21	26.90
Ni	8.64	4.78
	100.00	100.00

(b)

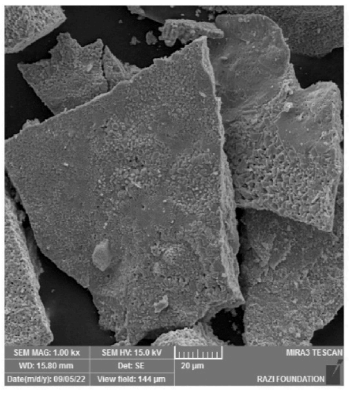

Elt	W%	A%
O	27.39	56.56
Al	0.17	0.21
Si	0.13	0.15
Cr	9.47	6.02
Mn	3.26	1.96
Fe	54.83	32.43
Ni	4.75	2.67
	100.00	100.00

Fig. 10. SEM image and EDS analysis of oxides stripped from the surface of (a) SLM and (b) wrought samples at a temperature of 800 °C.

the wrought alloy at 800 °C. As can be seen on the surface of the detached pieces of oxide, there is hilly and preferential growth in some places, the thickening of which can weaken the bond with the substrate and eventually lead to the oxide scale flaking off at that point. The EDS results also indicate that the composition of the detached oxides in the alloy after 100 h of oxidation are relatively the same, suggesting that iron oxide has less adhesion and can be detached during oxidation in both alloys. But the important point is that the amount of chromium element in the detached oxides in the SLM alloy is greater than in the wrought alloy, indicating that the spallation of the oxide layers has caused more useful oxides such as chromium oxide to fall off in the SLM alloy, and these falls cause the oxidation resistance of this alloy to be further reduced at a temperature of 800 °C. It appears that the finer grains in the SLM alloy compared to the wrought alloy as discussed in Fig. 1, and the lower amount of manganese in the composition have increased the oxidation rate of the SLM alloy. Moreover, the predominance of iron oxide in the composition of the oxide layer at this temperature has led to more spallation in the SLM alloy, which has led to an exponential increase in the oxidation rate.

To further investigate the reason for the difference in spallation rate

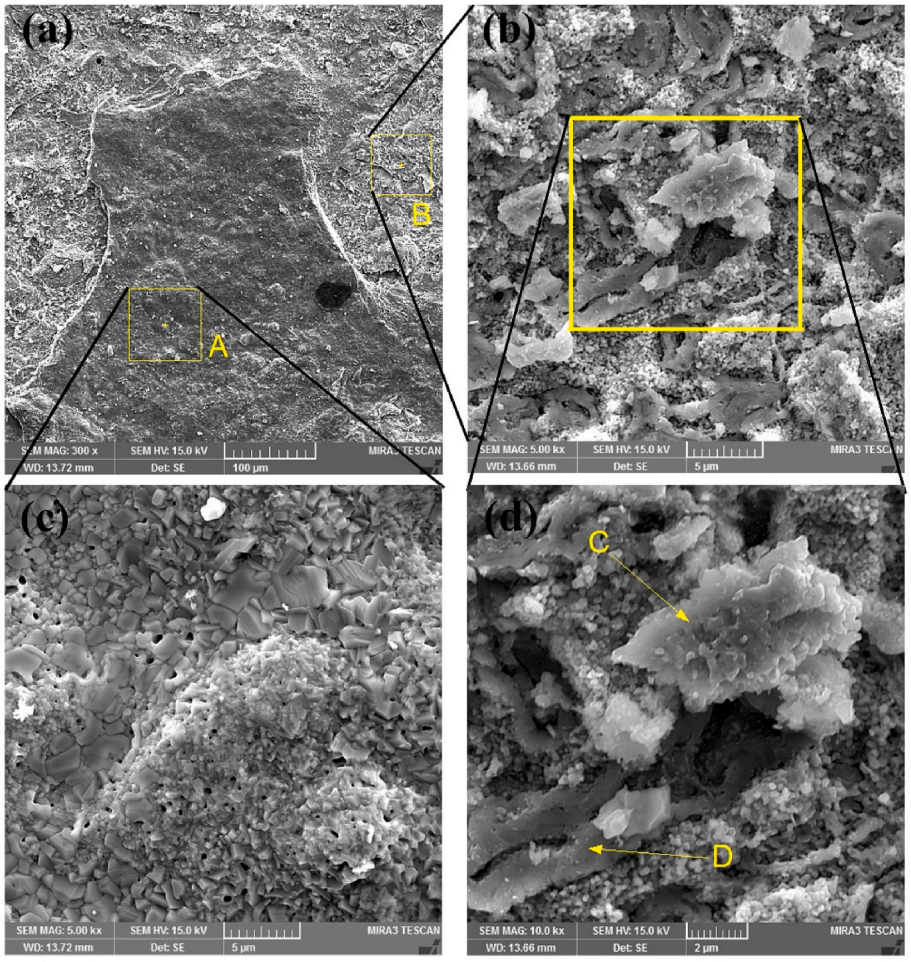

Elt	W%	A%
O	33.47	63.90
Si	0.06	0.07
Cr	1.13	0.66
Mn	5.89	3.27
Fe	46.13	25.23
Ni	12.98	6.75
Mo	0.34	0.11
	100.00	100.00

Region A

Elt	W%	A%
O	40.70	69.82
Si	1.45	1.42
Cr	32.30	17.05
Fe	10.01	4.92
Ni	12.76	5.96
Cu	0.29	0.12
Mo	2.49	0.71
	100.00	100.00

Region B

Elt	W%	A%
O	34.25	65.25
Si	0.65	0.71
Cr	27.49	16.12
Mn	0.66	0.36
Fe	16.38	8.94
Ni	10.30	5.35
Mo	10.27	3.26
	100.00	100.00

Region C

Elt	W%	A%
O	40.70	69.82
Si	1.45	1.42
Cr	32.30	17.05
Fe	10.01	4.92
Ni	12.76	5.96
Cu	0.29	0.12
Mo	2.49	0.71
	100.00	100.00

Region D

Fig. 11. (a) Top surface image of the oxide layer of the SLM sample oxidized at 800 °C for 100 h, (b) higher magnification image of the area where oxide spallation has occurred, (c) higher magnification image of the area that has not yet detached, (d) higher magnification image of a specified region of the figure in part (b), and (e) the results of the EDS analysis of the labelled regions in the figure.

between the two samples, the top surface of the oxide layer of the SLM sample was examined in the region where there is both a stripped and non-stripped surface. Fig. 11 shows an example of this region in the top surface of the SLM sample after 100 h at 800 °C. Fig. 11-(a) at low magnification clearly shows the hillock growth of the oxide surface in the SLM sample prior to spallation. The higher magnification image in the area where the oxide layer has been removed (area B) shows the cut oxide grains, which have the appearance of brittle fracture due to the low toughness of metal oxides. By further increasing the magnification in the part that has not yet detached (area A), it can also be seen that these areas, which appear as hills on the surface at low magnification, consist of angular oxide particles with pores and porosity between them. Many of these can be seen to provide a pathway for oxygen atoms to penetrate the substrate and increase the rate of oxidation in the SLM sample. This figure also shows the elemental analysis of region A (the region where the oxide has not yet detached) and region B (the region where the surface oxide has detached). By comparing the analysis of these two regions, the surface oxide that grows in hills and then falls is an iron-rich oxide. In fact, in the area where the hillocks have formed, the concentration of iron has increased in all samples, showing that the increase in the oxidation rate of this element leads to more intense formation of hillocks in the oxide scale and more fall. Fig. 11-d is a higher magnification image of Fig. 11-b, which shows more clearly that there are particles with a different appearance from the matrix, labelled C and D. The EDS analysis of these particles is also shown in section 10-e. From this analysis, these particles contain a significant amount of chromium, manganese and nickel and a small amount of iron. In other words, in this region, the oxide layer contains a background with a dominant composition of iron oxide and discontinuous segregated oxides containing other elements. This shows that prior to the formation of a uniform oxide on the surface of the SLM sample at 800 °C, the scale begins to detach as the oxide becomes hilly and its adhesion to the substrate decreases. As a result, the re-oxidation of the substrate has caused a sharp increase in the oxidation rate. This interpretation provides a good explanation for the shape of the graph of mass gain versus time for the SLM alloy at 800 °C (Fig. 3). In this figure it was observed that at the initial oxidation times the oxidation curve of the SLM alloy at 800 °C is very similar and close to the oxidation at 600 °C. As discussed earlier, the dominant composition in the oxide layer of the SLM alloy at 600 °C was iron oxide. The difference is that due to the higher oxidation kinetics of iron at 800 °C and the greater difference between the thermal conductivity coefficients of oxide and substrate at 800 °C compared to 600 °C, the adhesion of the oxide scale to the substrate is less and has caused the spallation of iron oxide hillocks at 800 °C. As a result of this phenomenon, a step-like curve can be interpreted in the oxidation of the SLM sample at 800 °C (Fig. 3).

For a more detailed study on the spallation phenomena, grazing tests were carried out on the SLM and wrought samples after 35 h oxidation at 800 °C, which were prepared separately. The reason for this was that this period was immediately prior to the dramatic increase in the amount of mass gain for the SLM sample compared to the wrought sample (Fig. 3). Fig. 12 presents the grazing results of this analysis on two samples. Comparison of the two XRD patterns shows that the oxide products for the wrought piece after 35 h of oxidation includes Fe_2MnO_4 and Fe_2O_3 and Fe_3O_4 phases, whereas there are only FeO peaks in the SLM specimen. The other difference with the 100-h grazing patterns is that here the FeO phase rather than the Fe_3O_4 phase is noticeable in the structure of the oxide layer, which may be due to the shorter oxidation period, as the abundance of oxygen in the oxide compounds Fe_2O_3 and Fe_3O_4 is greater than the proportion of oxygen in FeO. The non-presence of iron and manganese complex oxide in the phase configuration of the oxide layer for the SLM alloy after 35 h is an important point. It implies that the oxide layer of this alloy was almost free of manganese oxide just before the start of the stage of increased oxidation and severe spallation of the oxide layer. It was mentioned earlier that manganese has a positive effect on the protectiveness of the oxide layer. Therefore, the oxide layer of the SLM alloy has a higher diffusion rate than the oxide layer on the surface of the wrought sample and this has caused a higher tendency for hilly growth of the oxide layer, which can simultaneously lead to higher spallation and higher mass gain as observed in the kinetic diagram (Fig. 3). Furthermore, the plot of the wrought sample at 800 °C (Fig. 3) is consistent with the results presented here (Fig. 12-(b)). Initially, the oxidation rate of this sample exceeded that of the SLM sample in the early hours, resulting in the formation of iron oxide phases with a higher oxygen contribution (Fe_2O_3 and Fe_3O_4 compared to FeO). However, due to the non-hilly growth of these phases and the formation of the manganese containing oxide phase (Fe_2MnO_4), a protective oxide layer has formed on the surface.

Fig. 13 shows the top view of the oxidized surface of the wrought s sample at a temperature of 800 °C after 100 h. The arrows in this figure indicate the increase in magnification of the images. The microstructure of the oxide scale of the wrought alloy is completely different from that of the SLM alloy (Fig. 11). A smooth layer has formed on the surface, referred to as region A, and magnifications of this zone have been displayed up to 10,000 times. As can be seen, the microstructure of the oxide scale of the wrought alloy consists of angular particles, but with a high-density level, so that no void formation could be spotted within the oxidation surface. It is also observed that the tendency to form oxide hillocks with preferential growth in certain areas observed on the surface of the SLM sample is very low in the wrought sample. The results

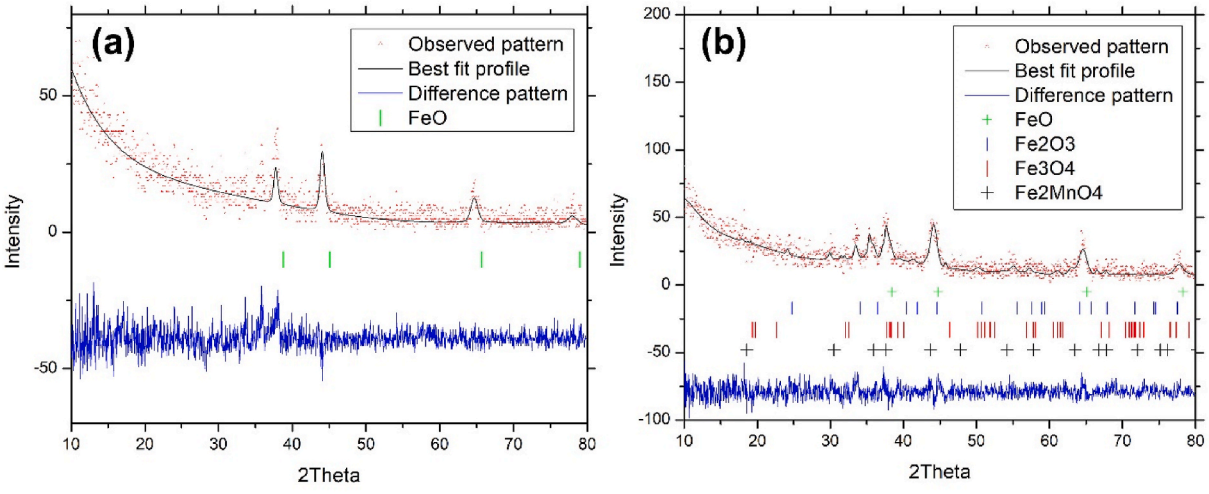

Fig. 12. Grazing incidence X-ray diffraction patterns along with Rietveld analysis of (a) SLM and (b) wrought samples at 800 °C after 35 h.

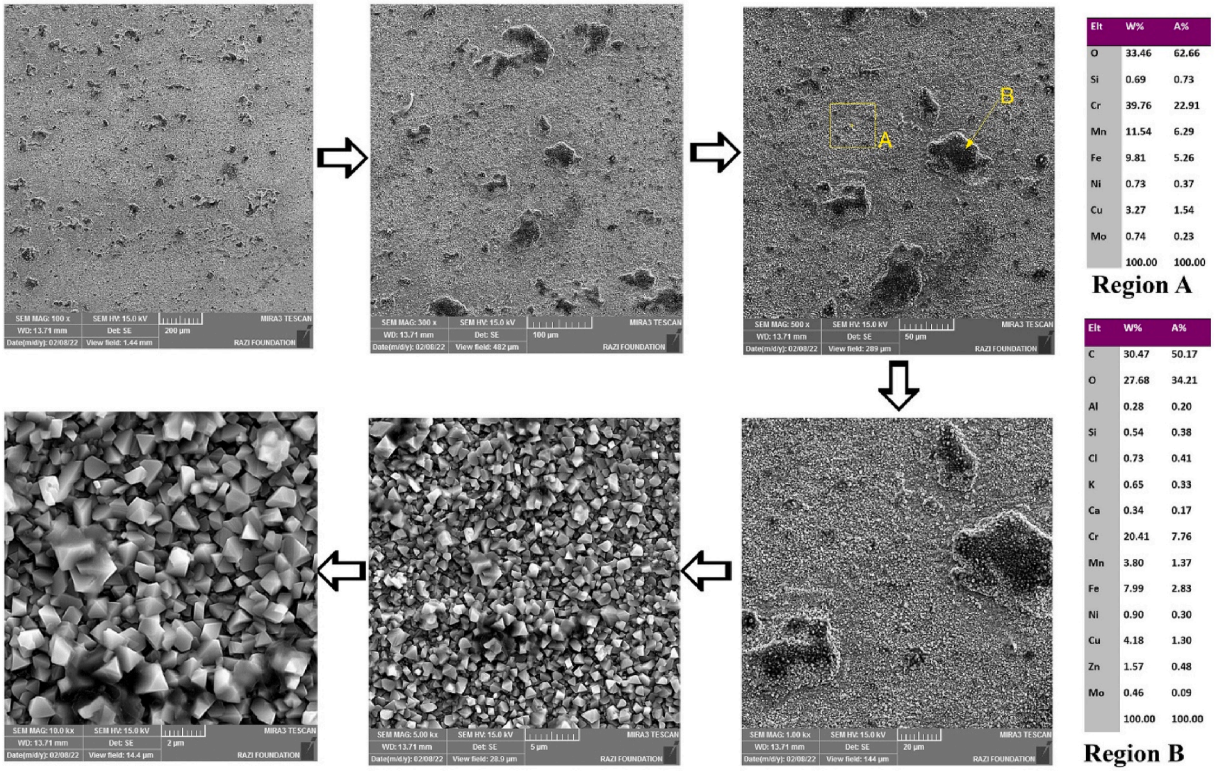

Fig. 13. The top view of the oxidized surface of the wrought sample at 800 °C after 100 h together with the EDS analysis of the labelled areas. The arrows indicate the direction of increasing magnification of the image.

show that the area marked A in the oxide layer of the wrought sample has a relatively high amount of chromium (about 40%) and manganese (about 10%) and a low amount of iron. The areas marked B in the microstructure do not differ significantly from areas A and it is only in these areas that more contamination has been absorbed after the end of oxidation, changing the compositional balance of these areas. However, the ratio of 4 times Cr to Fe is also seen in these areas, showing that these areas are not significantly different from other areas. The notable presence of chromium in the oxide layer of the wrought sample, together with a higher concentration of manganese compared to the SLM alloy after 100 h at a temperature of 800 °C, is consistent with the results of the grazing test (Fig. 7(d)) and the oxidation kinetic results (Fig. 3). In fact, the results of the microstructural study and the grazing test confirm that, at this temperature, the difference in oxidation behavior between the two samples is the result of the formation of Fe_2MnO_4 in the early stage of exposure and the continuous formation of an oxide layer containing CrO_3 in the remaining time of up to 100 h on the surface of the wrought alloy.

Finally, regarding the temperature of 900 °C, as mentioned in the explanation of Figs. 6–8, the most important factors affecting the reduction of the oxidation rate are the increase in the amount of chromium and manganese in the oxide layer and the formation of a continuous oxide scale which acts as a barrier to oxygen penetration. For a more accurate validation of this analysis, the top view of oxidized samples at this temperature was also examined. Fig. 14 shows the top view of the oxidized surface of the wrought alloy at a temperature of 900 °C after 100 h. In the first part of this figure the uniformity of the oxide layer formed on the surface can be clearly seen. The few places where hillock-like growth can be seen are shown at two higher magnifications in this figure. In contrast to the 800 °C temperature, the lack of excessive growth of oxide hillocks was one of the most important factors in reducing the spallation of the oxide scale at this temperature. The EDS analysis consists of the matrix of the oxide layer (labelled A) and one of the few places where there is hilly growth (labelled B) is also shown in the figure. The result of the matrix analysis confirms the previous interpretation of a significant increase in the amount of chromium and a relative increase in the amount of manganese in the oxide layer. The analysis of region B in the figure also shows that preferential and non-uniform growth occurs where the amount of iron in the oxide layer is higher. This is also consistent with the previous findings mentioned in this article. In fact, the formation of complex oxides rich in chromium and manganese on the surface of the oxide layer at 900 °C not only contributes to the formation of a comparatively protective barrier against further oxygen penetration, but also leads to a reduction in the amount of iron oxide within the oxide layer. As a result, there is a significant reduction in the occurrence of hilly growth and subsequent detachment of the oxide layer.

4. Conclusions

1 A comparison of the oxidation behavior of 316L steel in SLM and wrought condition in the temperature range of 600 °C–900 °C shows that the SLM alloy has a lower oxidation resistance, especially at 800 °C. The main reasons are the increase in penetration paths due to the reduction in grain size and the lower amount of chromium and manganese in the oxide layer of the SLM alloy compared to the wrought sample. The results indicate that a reduced presence of alloying elements critical for oxidation, particularly chromium and manganese, in the composition of the SLM alloy can result in the failure to form phases that increase oxidation resistance, such as Cr_3O and Fe_2MnO_4, particularly at 800 °C. This consequently accelerates the oxidation rate of the SLM alloy.

2 The oxidation kinetics in both SLM and wrought conditions are close to each other at 600 °C and in both alloys iron oxide dominates in the oxide layer and the amount of chromium present in is low. At this temperature, preferential hillock growth is observed in the oxide scale, but the amount of oxidation and the stresses resulting from

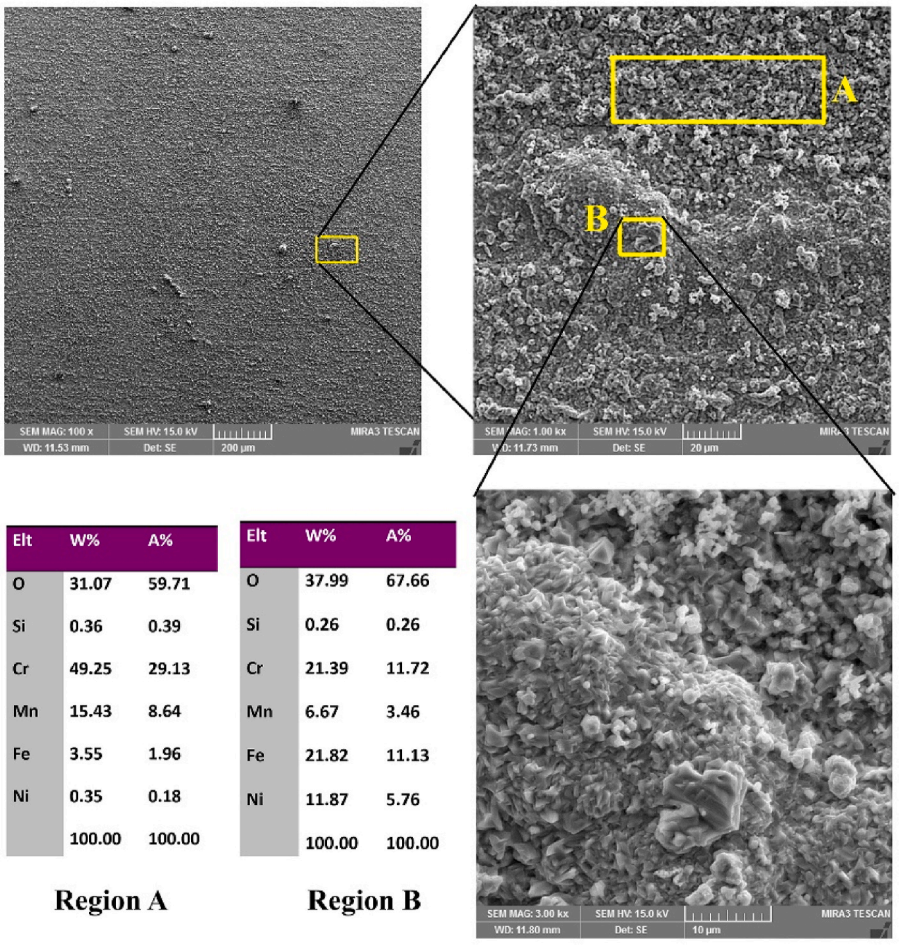

Elt	W%	A%
O	31.07	59.71
Si	0.36	0.39
Cr	49.25	29.13
Mn	15.43	8.64
Fe	3.55	1.96
Ni	0.35	0.18
	100.00	100.00

Region A

Elt	W%	A%
O	37.99	67.66
Si	0.26	0.26
Cr	21.39	11.72
Mn	6.67	3.46
Fe	21.82	11.13
Ni	11.87	5.76
	100.00	100.00

Region B

Fig. 14. The top view image of the oxide layer of the wrought alloy oxidized at 900 °C for 100 h together with enlarged images of the few areas where there was hillock growth; and also the EDS analysis of the labelled areas in the figure.

hillock growth are not at a level to result in significant spallation of the oxide scale.

3 At the temperature of 800 °C, the oxidation rate is higher in both alloys since the increase in temperature causes an increase in the oxidation rate, but the formation of a uniform oxide layer containing complex oxide phase on the surface occurs only in the wrought sample and with compositions of Cr_3O and Fe_2MnO_4. Meanwhile, in the SLM sample, the difference in the oxidation rate due to the difference in the initial microstructural conditions causes the initial growth of the iron oxide in the form of a hillock, without any significant presence of chromium in the alloy, and as a result it causes the detachment of the oxide scale. This increases the oxidation of this alloy due to exposure to the substrate and makes the mass gain curve stepwise and exponential.

4 At the temperature of 900 °C, the oxidation rate in both SLM and wrought samples is reduced and a uniform oxide layer with a higher chromium and manganese content (with composition of $CrMnO_4$ and Fe_2MnO_4) is formed on the surface, resulting in better oxidation resistance in both samples. In fact, increasing the temperature up to 900 °C results in the preferential oxidation of chromium and manganese compared to iron on the surface of both alloys, and this leads to the absence of a dominant growth of iron oxide hillocks on the surface and prevents spallation of the oxide scale.

Declaration of competing interest

The authors declare that they have no known competing financial interests or personal relationships that could have appeared to influence the work reported in this paper.

Acknowledgements

Filipe Fernandes acknowledges the: UIDB/00285/2020 and LA/P/0112/2020 projects, sponsored by FEDER Funds through Portugal 2020 (PT2020), by the Competitiveness and Internationalization Operational Program (COMPETE 2020), and national funds through the Portuguese Foundation for Science and Technology (FCT).

References

[1] Gardner L. Metal additive manufacturing in structural engineering–review, advances, opportunities and outlook. In: Structures. Elsevier; 2023.
[2] Sharma SK, et al. Processing techniques, microstructural and mechanical properties of additive manufactured 316L stainless steel. J Inst Eng: Series 2023;D:1–14.
[3] Dandekar TR. A review on heat treatments, microstructure, and mechanical properties of selective laser-melted AISI 316L. Hybrid Metal Additive Manufacturing 2023:62–86.
[4] Liu J, et al. Effect of scanning speed on the microstructure and mechanical behavior of 316L stainless steel fabricated by selective laser melting. Mater Des 2020;186:108355.
[5] Yazıcı M, et al. Investigation of mechanical, tribological and magnetic properties after plasma nitriding of AISI 316L stainless steel produced with different orientations angles by selective laser melting. Surf Coating Technol 2023;467:129676.
[6] Amanov A. Effect of local treatment temperature of ultrasonic nanocrystalline surface modification on tribological behavior and corrosion resistance of stainless steel 316L produced by selective laser melting. Surf Coating Technol 2020;398:126080.
[7] Alvi S, Saeidi K, Akhtar F. High temperature tribology and wear of selective laser melted (SLM) 316L stainless steel. Wear 2020;448:203228.

[8] Huang Y, et al. Microstructure and wear properties of selective laser melting 316L. Mater Chem Phys 2020;254:123487.
[9] Hatami S, et al. Fatigue strength of 316 L stainless steel manufactured by selective laser melting. J Mater Eng Perform 2020;29(5):3183–94.
[10] Avanzini A. Fatigue behavior of additively manufactured stainless steel 316L. Materials 2022;16(1):65.
[11] Sefene EM. State-of-the-art of selective laser melting process: a comprehensive review. J Manuf Syst 2022;63:250–74.
[12] Gao B, Zhao H, Peng L, Sun Z. A review of research progress in selective laser melting (SLM). Micromachines 2022;14(1):57.
[13] Nezakat M, Akhiani H, Penttilä S, Szpunar J. Oxidation behavior of austenitic stainless steel 316L and 310S in air and supercritical water. J Nucl Eng Radiat Sci 2016;2(2):021008.
[14] de Moraes FP, Junior SFA, Plaut RL, Padilha AF. Degradation of microstructure and properties of an AISI 316L steel pipe after more than 100,000 hours usage at 640 C in a petrochemical industry. Procedia Struct Integr 2019;17:131–7.
[15] Chen R, Yeun W. Review of the high-temperature oxidation of iron and carbon steels in air or oxygen. Oxid Metals 2003;59(5):433–68.
[16] Huang X, et al. Oxidation behavior of 316L austenitic stainless steel in high temperature air with long-term exposure. Mater Res Express 2020;7(6):066517.
[17] Buscail H, et al. Role of molybdenum on the AISI 316L oxidation at 900 C. J Mater Sci 2008;43(21):6960–6.
[18] Buscail H, et al. Characterization of the oxides formed at 1000 C on the AISI 316L stainless steel—role of molybdenum. Mater Chem Phys 2008;111(2–3):491–6.
[19] Wood GC. The oxidation of iron-chromium alloys and stainless steels at high temperatures. Corrosion Sci 1962;2(3):173–96.
[20] Monceau D, Vilasi M. High temperature oxidation of additively manufactured structural alloys. J Miner Met Mater Soc 2022;74(4):1659–67.
[21] Siri C, et al. Impact of selective laser melting additive manufacturing on the high temperature behavior of AISI 316L austenitic stainless steel. Oxid Metals 2020;94:527–48.
[22] Siri C, et al. Impact of water vapor on the high temperature oxidation of wrought and selective laser melted (SLM) AISI 316L. Oxid Metals 2021;96:347–59.
[23] Benafia S, et al. Influence of surface mechanical attrition treatment on the oxidation behaviour of 316L stainless steel. Corrosion Sci 2018;136:188–200.
[24] Dudziak T, et al. Effect of 316L stainless steel Fabrication on oxidation resistance, surface morphology, and hot tensile behavior. J Mater Eng Perform 2023;32(22):10443–54.
[25] Kim J-H, et al. Grain-size effects on the high-temperature oxidation of modified 304 austenitic stainless steel. Oxid Metals 2013;79:239–47.
[26] Yang Y, et al. Effect of grain size on oxidation resistance of unalloyed titanium. In: Materials Science forum. Trans Tech Publ; 2017.
[27] Trindade VB, et al. Effect of alloy grain size on the high-temperature oxidation behavior of the austenitic steel TP 347. Mater Res 2005;8:371–5.
[28] Ronqueti LA, Favergeon J, Risbet M, Picard M. Study of grain boundary oxidation of high alloyed carbon steels at coiling temperature. 53th Seminario de Laminacao 2016:283–92.
[29] Sanviemvongsak T, Monceau D, Desgranges C, Macquaire B. Intergranular oxidation of Ni-base alloy 718 with a focus on additive manufacturing. Corrosion Sci 2020;170:108684.
[30] Casati R, Lemke J, Vedani M. Microstructure and fracture behavior of 316L austenitic stainless steel produced by selective laser melting. J Mater Sci Technol 2016;32(8):738–44.
[31] Mertens A, et al. Microstructures and mechanical properties of stainless steel AISI 316L processed by selective laser melting. In: Materials science forum. Trans Tech Publ; 2014.
[32] Jiang H-Z, et al. Effect of process parameters on defects, melt pool shape, microstructure, and tensile behavior of 316L stainless steel produced by selective laser melting. Acta Metall Sin 2021;34:495–510.
[33] Saeidi K, et al. 316L stainless steel designed to withstand intermediate temperature. Mater Des 2017;135:1–8.
[34] Andreatta F, et al. Corrosion behaviour of 316L stainless steel manufactured by selective laser melting. Mater Corros 2019;70(9):1633–45.
[35] Moroishi T, Fujikawa H, Makiura H. The effect of carbon, zirconium, niobium, and titanium on the oxidation resistance of chromium stainless steel. J Electrochem Soc 1979;126(12):2173.
[36] Rawers J. Oxidation characteristics of Fe–18Cr–18Mn-stainless steel alloys. Oxid Metals 2010;74:167–78.
[37] Zhang X, Yocom CJ, Mao B, Liao Y. Microstructure evolution during selective laser melting of metallic materials: a review. J Laser Appl 2019;31(3).
[38] Basirat M, Isfahani T, Hadi M. Implementing shear-punch test for the assessment of mechanical properties of cast and selective laser melted AlSi10Mg alloys. Progress in Additive Manufacturing 2024:1–17.
[39] Sola A, Nouri A. Microstructural porosity in additive manufacturing: the formation and detection of pores in metal parts fabricated by powder bed fusion. Journal of Advanced Manufacturing and Processing 2019;1(3):e10021.
[40] Ishikawa Y, Odaka K. Reduction of outgassing from stainless surfaces by surface oxidation. Vacuum 1990;41(7–9):1995–7.
[41] Hadi M, et al. Oxidation properties of a beta-stabilized TiAl alloy modified by rare earth elements. Oxid Metals 2018;90:421–34.
[42] Karimi H, Ghasemi A, Hadi M. Microstructure and oxidation behaviour of TiAl (Nb)/Ti 2 AlC composites fabricated by mechanical alloying and hot pressing. Bull Mater Sci 2016;39:1263–72.
[43] Hadi M, Rafiaei SM, Fernandes F. The effect of Mo2C additions on the oxidation resistance of (Ti, W) CN cermets as base material for the production of cutting tools. Ceram Int 2023;49(13):21538–45.
[44] Karimi H, et al. High-temperature oxidation behaviour of WC-FeAl composite fabricated by spark plasma sintering. Ceram Int 2018;44(14):17147–53.